Eur. Phys. J. D (2024) 78:122
https://doi.org/10.1140/epjd/s10053-024-00914-7

THE EUROPEAN PHYSICAL JOURNAL D

Regular Article - Atomic Physics

Breit interaction in dielectronic recombination of hydrogenlike xenon ions: storage-ring experiment and theory

Shu-Xing Wang[1,2], Carsten Brandau[1,3], Stephan Fritzsche[3,4,5], Sebastian Fuchs[1,2], Zoltán Harman[6,7], Christophor Kozhuharov[3], Alfred Müller[1], Markus Steck[3], and Stefan Schippers[1,2,a]

[1] I. Physikalisches Institut, Justus-Liebig-Universität Gießen, 35392 Giessen, Germany
[2] Helmholtz Forschungsakademie Hessen für FAIR (HFHF), GSI Helmholtzzentrum für Schwerionenforschung, Campus Gießen, 35392 Giessen, Germany
[3] GSI Helmholtzzentrum für Schwerionenforschung, 64291 Darmstadt, Germany
[4] Helmholtz-Institut Jena, 07743 Jena, Germany
[5] Institut für Theoretische Physik, Friedrich-Schiller-Universität Jena, 07743 Jena, Germany
[6] Institut für theoretische Physik, Justus-Liebig-Universität Gießen, 35392 Giessen, Germany
[7] Max-Planck-Institut für Kernphysik, 69117 Heidelberg, Germany

Received 24 July 2024 / Accepted 11 September 2024 / Published online 1 October 2024

Abstract. Electron-ion collision spectroscopy of the KLL dielectronic recombination (DR) resonances of hydrogenlike xenon ions was performed at a heavy-ion storage ring with a resolving power that is competitive with x-ray spectroscopy of inner-shell transitions in highly charged ions. The $KL_{1/2}L_{1/2}$, $KL_{1/2}L_{3/2}$, and $KL_{3/2}L_{3/2}$ resonance groups and even parts of their fine structure are individually resolved. The resonance strengths were measured on an absolute scale and compared with results from multi-configuration Dirac–Fock (MCDF) calculations. These are in excellent agreement with the experimental findings when QED effects on the resonance energies and the Breit interaction are considered. As already found for DR of hydrogenlike uranium (Bernhardt et al. in Phys Rev A 83:020701(R), 2011), this interaction is particularly strong for the $KL_{1/2}L_{1/2}$ resonance group. For U^{91+}, it increases the $KL_{1/2}L_{1/2}$ DR resonance strength by 40%. For Xe^{53+}, the increase is found to amount to 25%, confirming the prediction that the influence of the Breit interaction grows with increasing nuclear charge. A comprehensive appendix treats the derivation of experimental and theoretical merged-beams recombination rate coefficients for interacting beams of relativistic electrons and ions.

1 Introduction

Highly charged ions provide a unique test bench for relativistic and quantum electrodynamics (QED) effects. Using an energetic electron beam as a probe, one can study the inelastic interactions between electrons and ions including excitation, ionization and recombination. In the present work, we focus on electron-ion recombination processes. Recombination of a free electron and an atomic ion can proceed via two pathways: direct nonresonant radiative recombination (RR) and dielectronic recombination (DR), which is a resonant two-step process. In the first step, the parent ion (at an initial level i) is resonantly excited by capture of a free electron into a bound level, forming a doubly excited product ion. In the second step, the doubly excited intermediate level d may decay either via autoionization back to the initial charge state of the ion or radiatively via photon emission, thus stabilizing the charge state of the recombined ion. Accordingly, the DR strength S^{DR} is determined by the product of the resonant capture rate and the radiative branching ratio of the intermediate state, i.e.,

$$S^{\mathrm{DR}} \propto A^{\mathrm{DC}}_{i\to d}\,\frac{A^{r}_{d\to f}}{\sum_{f'} A^{r}_{d\to f'} + \sum_{j} A^{a}_{d\to j}}. \qquad (1)$$

Here, $A^{\mathrm{DC}}_{i\to d}$ is the dielectronic capture (DC) rate, which is proportional to the Auger rate $A^{a}_{d\to i}$ for the time-inverse process, $A^{r}_{d\to f}$ indicates the radiative decay rate to a final level f below the ionization threshold, $A^{a}_{d\to j}$ represents the autoionization rates, and the denominator corresponds to the natural width of the DR resonance. The summations extend over all levels f' and j that can be reached from level d either radiatively or by autoionization, respectively. KLL DR refers to the excitation of a bound K-shell electron into the L-shell, while the initially free electron is also captured into the L shell.

[a] e-mail: schippers@jlug.de (corresponding author)

Nonrelativistically, the Auger rates are largely independent of Z while the radiative rates scale approximately with Z^4. In light (low-Z) ions autoionization rates are therefore usually much larger than radiative rates. Then, the Auger rates cancel in the calculation of the DR strengths (Eq. 1) and the latter are dominated by the radiative rates. With increasing nuclear charge Z, radiative stabilization becomes comparable to and even faster than autoionization of the doubly excited levels. As a consequence, the DR strengths in heavy ions is highly sensitive to the Auger rates and, hence, to the electronic correlations in the doubly excited system. The dominant part of this interaction is due to the Coulomb potential

$$V^{\mathrm{C}} = \frac{e^2}{4\pi\varepsilon_0}\frac{1}{|\vec{r}_1 - \vec{r}_2|} = \frac{e^2}{4\pi\varepsilon_0}\frac{1}{r_{12}} \tag{2}$$

in the Auger matrix elements with r_{12} being the distance between the two electrons, e the elementary charge and ϵ_0 the vacuum permittivity. In the relativistic domain, magnetic interactions [1] and retardation effects [2] have to be accounted for in addition. The corresponding potential term is [3,4]

$$V^{\mathrm{B}}(\omega) = -\frac{e^2}{4\pi\varepsilon_0}\left[\vec{\alpha}_1\cdot\vec{\alpha}_2\frac{\cos(\omega r_{12}/c)}{r_{12}} + (\vec{\alpha}_1\cdot\vec{\nabla}_1) \times(\vec{\alpha}_2\cdot\vec{\nabla}_2)\frac{\cos(\omega r_{12}/c)-1}{\omega^2 r_{12}/c^2}\right]. \tag{3}$$

This (pairwise) two-electron potential is commonly referred to as the Breit interaction and can be interpreted as being mediated by the exchange of a virtual transverse photon with frequency ω. In Eq. 3, the Cartesian components of the vectors $\vec{\alpha}_1$ and $\vec{\alpha}_2$ are the Dirac matrices, and c denotes the speed of light. The importance of the Breit interaction generally increases with Z. For $Z \gtrsim 50$, a strong Z scaling of the Breit contribution was theoretically predicted, e.g., for heliumlike and neonlike ions [5,6].

Experimental work addressing the Breit interaction has been reviewed by Nakamura [7]. Therefore, we only briefly mention here that evidence for the influence of the Breit interaction on DR resonance strengths has been provided previously by ion atom collision experiments [8,9] and by measurements with heavy lithiumlike ions at the Tokyo-EBIT [10]. Later studies have additionally investigated electron-impact excitation [11] as well as the angular distributions [12,13] and the polarization [14,15] of the emitted radiation from the DR process, confirming earlier theoretical predictions [16] of the importance of the Breit interaction also for these more differential quantities.

A drawback of DR measurements at EBITs is that the measured cross sections are not on an absolute scale, since the trap usually contains a mixture of charge states and since the number of trapped ions in the charge state of interest is not known sufficiently well. Quantitative DR cross-section measurements can be conducted with the electron-ion merged-beams method as implemented at heavy-ion storage rings with electron coolers [17,18]. Such measurements pose even more stringent tests of the theoretical calculations than relative cross-section measurements alone. The experimental challenge lies in the realization of the comparatively high electron-ion collision energies which are required for accessing KLL DR resonances in highly charged ions.

In the usual storage-ring approach (see, e.g., [19–22]), the electron cooler serves for cooling of the ion beam and also as an electron target, where electron-ion recombination occurs. For realizing nonzero electron-ion collision energies, the electron energy has to be tuned away from the cooling condition. Due to the merged-beams kinematics, large changes of the electron energy in the laboratory frame result in only small changes of the collision energy, such that the maximum collision energy is limited by the voltage range of the cooler power supplies to much lower values than what is required for measuring KLL DR.

In order to realize high electron-ion collision energies, a novel approach was introduced at the heavy-ion storage-ring ESR, operated by GSI in Darmstadt, Germany, where the ion beam was cooled stochastically [23], and the electron beam was used exclusively as an electron target. This permitted a free choice of the electron energy, such that electron-ion collision energies of up to 90 keV could be realized [24] and absolute rate coefficients for KLL and KLM DR of hydrogenlike U^{91+} could be measured [25]. Detailed comparisons with theoretical calculations revealed strong contributions by the Breit interaction of up to 44% to the absolute DR resonance strengths.

Here, we present absolute rate coefficients for KLL DR of hydrogenlike Xe^{53+} using the stochastic cooling technique and the electron cooler at the ESR. The measured data are compared with multi-configuration Dirac–Fock (MCDF) calculations with and without inclusion of the Breit interaction. The paper is organized as follows. In Sect. 2, we describe the experimental aspects, including the procedures, parameters and data analysis. The theoretical method is described in Sect. 3. The results are compared and discussed in Sect. 4. A summary of the results is given in Sect. 5. Two comprehensive appendices provide details of the comparison between experimental and theoretical merged-beams rate coefficients by employing a Monte Carlo approach.

2 Experimental procedures

The experiment was performed at the experimental storage ring (ESR) of the GSI Helmholtzzentrum für Schwerionenforschung (GSI) in Darmstadt, Germany. Hydrogenlike $^{136}Xe^{53+}$ ions provided by the GSI accelerator chain were injected into the ESR at an energy of about 400 MeV/u. Stochastic cooling [23] was applied to reduce the ion beam diameter and the momentum spread of the ions.

In typical electron-ion merged-beams experiments, where the ion beam is cooled by means of electron cooling, the momentum spread of the ion beam is typically $\delta p/p < 10^{-4}$ [26,27] and does not contribute to the collision-energy spread. The experimental resolving power and the DR resonance line shapes are then governed by the properties of the electron beam, namely its transverse and longitudinal temperatures, $T_\perp$ and $T_\parallel$, respectively [28]. For a stochastically cooled ion beam as in the present experiment, its momentum spread typically exceeds the one from an electron-cooled ion beam by up to a factor of five. Since the quality of the stochastic cooling depends on the number of stored particles and on the applied power, we kept the momentum spread of the ion beam at or below 2×10^{-4} by limiting the intensity of the ion beam to about 800 μA corresponding to $N_i = 5.7 \times 10^7$ stored ions for all experimental runs.

In principle, higher beam intensities of up to more than 3 mA could be accumulated, but were not used in the data-taking runs since such high beam intensities entailed ion momentum spreads $\delta p/p > 5 \times 10^{-4}$, which deteriorated the experimental energy resolution. It should be noted that the momentum spread of $\delta p/p \approx 2 \times 10^{-4}$ is about a factor of four smaller than in our previous experiment with U^{91+} ions, where the beam was stochastically cooled only *before* the data taking, bunched with the ESR radio frequency (RHF) and decelerated from the injection orbit to the central ESR orbit. The operability of this method was considerably easier as compared to the present one, but keeping the beam energy constant with the ESR RF resulted, as expected, in a four times higher relative momentum spread of the uranium beam as compared to the one of the present xenon beam, which was stochastically cooled continuously also *during* the data taking. In order to achieve this, an iterative optimization of the ion optics of the ring had to be performed, which comprised a shift of the ion orbit in order to render possible the detection of the recombined Xe^{52+} ions. Subsequently, the delay between the pickup and the kicker of the stochastic cooling had to be carefully readjusted.

The beam lifetime of the Xe^{53+} ions at 400 MeV/u was several hours, and hence was constant over the typical duration of 440 s for an DR energy scan. Normally, at the high ion energy of 400 MeV/u, using a very highly charged ion such as Xe^{53+}, the dominant loss mechanism would be electron cooling and rather than collisions with residual-gas particles of the ultrahigh vacuum in the storage ring. Thus, a further benefit of experiments with solely stochastically cooled ion beam are the practically constant experimental ion beam conditions.

The ESR electron cooler provided an electron beam with an electrical current of 500 mA, corresponding to a number density $n_e \approx 9.4 \times 10^6$ cm^{-3} in the laboratory system. The recombined ions were separated from the primary ion beam in the first bending magnet and detected by a gas counter with nearly 100% efficiency ($\eta \leq 1$). From the recorded count rate $R_{\rm exp}$ of recombined Xe^{52+} ions, the *absolute* merged-beams recombination rate coefficient was calculated as (see appendix A)

$$\alpha_{\rm mb}(E_{\rm cm}) = \frac{R_{\rm exp} C}{\eta(1-\beta_e\beta_i) L N_i n_e}, \tag{4}$$

with merged-beams overlap length $L = 2.5$ m in the ESR electron cooler and the circumference $C = kC_0$ of the ion orbit, where $C_0 = 108.36$ m is the nominal length of the central ESR orbit and the coefficient k accounts for the previously mentioned shift of the actual ion orbit. Its not precisely known (small) deviation from unity contributes to the error budget presented below. The quantities $\beta_e = v_e/c$ and $\beta_i = v_i/c$ in the relativistic factor $(1-\beta_e\beta_i)$ denote the electron and ion velocities in the laboratory frame in units of the vacuum speed of light. From these, the electron-ion collision energy in the center-of-mass frame can be calculated as [19]

$$E_{\rm cm} = m_i c^2 (1+\mu) \left[\sqrt{1 + \frac{2\mu(\gamma_{\rm rel}-1)}{(1+\mu)^2}} - 1 \right], \tag{5}$$

with the ratio $\mu = m_e/m_i \ll 1$ of the electron and ion rest masses,

$$\gamma_{\rm rel} = \gamma_e \gamma_i (1 - \beta_e \beta_i \cos\theta), \tag{6}$$

$\gamma_e = (1-\beta_e^2)^{-1/2}$, $\gamma_i = (1-\beta_i^2)^{-1/2}$, and the angle θ between the ion and electron beams. Both beams were adjusted such that $\theta = 0$ was realized with an estimated uncertainty $\Delta\theta = \pm 0.5$ mrad.

The electron energy is determined by the cathode and drift tube voltages $U_{\rm cath}$ and $U_{\rm dt}$ (both relative to ground potential), respectively, and by the space-charge potential $U_{\rm sc}$ on the axis of the electron beam relative to the drift tube potential. Accordingly, the Lorentz factor γ_e can be expressed as

$$\gamma_e = 1 + \frac{-eU_{\rm cath} + eU_{\rm dt} + eU_{\rm sc}}{m_e c^2}. \tag{7}$$

During the measurement, the cathode voltage was set to a center value of -97864 V and the electron energy was scanned by swiftly switching $U_{\rm dt}$ as described in Ref. [29], albeit with a slightly different timing pattern. Over the experimental electron energy range, the space-charge potential was calculated [30] to be -103 V.

The actual voltages were measured with a precision high-voltage probe, and the set voltages were corrected accordingly. Calibration measurements were carried out repeatedly and differed on the 2×10^{-4} level. We therefore assign an uncertainty of $\Delta E_e/E_e = \pm 2 \times 10^{-4}$ to the laboratory electron energy corresponding to $\Delta E_e = \pm 20$ eV at $E_e = 100$ keV.

The ion energy was calibrated by switching the stochastic cooling off and by then cooling the ion beam with the electron cooler instead. The acceleration volt-

age of the electron beam was set such that it resulted in the same revolution frequency of the ions as had been achieved with stochastic cooling before. The resulting 'cooling voltage' was $U_{\rm cool} = -220033\ V$. To experimentally achieve the electron cooling condition, $U_{\rm cath} = U_{\rm cool}$ and $U_d = 0$ V were used. At these settings, the space-charge potential was $U_{\rm sc-cool} = -78$ V, i.e., the electron energy at cooling was $E_{\rm cool} = -eU_{\rm cool} + eU_{\rm sc-cool} = 219955$ eV. To this value, the same calibration error applies as above, i.e., $\Delta E_{\rm cool}/E_{\rm cool} = \pm 2 \times 10^{-4}$ or $\Delta E_{\rm cool} = \pm 44$ eV. Thus, the determined ion energy was $E_i = (m_u/m_e)E_{\rm cool} = 400.95 \pm 0.12$ MeV per nucleon with m_u denoting the atomic mass unit.

The uncertainties $\Delta\theta = \pm 0.5$ mrad, $\Delta E_e = \pm 20$ eV, and $\Delta E_{\rm cool} = \pm 44$ eV propagate to the uncertainty of $E_{\rm cm}$ (Eq. 5). Applying the usual error calculus, which involves the partial derivatives of $E_{\rm cm}$ with respect to θ, E_e, and $E_{\rm cool}$, and adding all errors in quadrature results in $\Delta E_{\rm cm} = \pm 16$ eV. The experimental uncertainty of the measured rate coefficient ($\pm 13\%$) results mainly from (see Eq. 4) the uncertainties in the number of stored ions ($\pm 5\%$), in the electron density ($\pm 10\%$), the length of the ion orbit ($\pm 5\%$) and detection efficiency (-5%) [25].

3 Theoretical method

We describe the relativistic two-electron states involved in the *KLL* DR process on the basis of the Dirac–Coulomb–Breit (DCB) Hamiltonian:

$$H^{\rm DCB}(\omega) = \sum_{i=1}^{2} h_i + \sum_{i<j}^{2} \left[V_{ij}^{\rm C} + V_{ij}^{\rm B}(\omega)\right] . \qquad (8)$$

Here, the one-particle operators are

$$h_i = c\vec{\alpha}_i \cdot \vec{p}_i + \left(\hat{\beta}_i - 1\right) m_e c^2 + V_{\rm nuc}(r_i) , \qquad (9)$$

with $\vec{p}_i$ being the relativistic momentum operator and $\hat{\beta}_i$ is the Dirac matrix acting on the four-component wave function of the ith particle. The nuclear model potential $V_{\rm nuc}$ describes the nuclear charge distribution as a two-parameter Fermi function.

The two-electron atomic state function (ASF) is given as a linear superposition of configuration state functions (CSFs) with common total angular momentum (J), magnetic (M) and parity (P) quantum numbers [31]:

$$|\Gamma PJM\rangle = \sum_{k=1}^{n_c} c_k |\gamma_k PJM\rangle . \qquad (10)$$

The CSFs $|\gamma_k PJM\rangle$ are constructed as jj-coupled Slater determinants of relativistic orbitals. The γ_k stands collectively for all the parameters needed to uniquely describe the CSF, i.e., occupation numbers and the angular momenta coupling scheme. The number of CSFs is denoted by n_c. Γ denotes the set of all the γ_k included in the representation of the ASF. We take the list of spectroscopic doubly excited states, given in Table 1, as the set of CSFs for the intermediate levels, and the $1s2l$ singly excited states for the representation of final states. The one-particle wave functions are characterized/classified by their principal quantum number $n = 1, 2$, the total angular momentum $j = |\kappa| - \frac{1}{2} = \frac{1}{2}, \frac{3}{2}$ and its projection μ:

$$\phi_{n\kappa\mu}(\vec{r}) = \frac{1}{r} \begin{pmatrix} P_{n\kappa}(r)\Omega_{\kappa\mu}(\hat{r}) \\ i\,Q_{n\kappa}(r)\Omega_{-\kappa\mu}(\hat{r}) \end{pmatrix} . \qquad (11)$$

Here, $\kappa = 2(l-j)\,(j+1/2)$ is the Dirac angular momentum quantum number with l being the orbital angular momentum, $P_{n\kappa}(r)$ and $Q_{n\kappa}(r)$ are the large and small radial wave functions, and the $\Omega_{\kappa\mu}(\hat{r})$ are the spherical spinors depending on the $\hat{r}$ unit vector [32].

In our calculations, the Coulomb part of the electron–electron interaction is treated self-consistently, i.e., the eigenvalues and eigenvectors of the Dirac–Coulomb Hamiltonian are approximated. The mixing coefficients c_k are determined by diagonalizing this Hamiltonian in the given CSF set. Simultaneously, the radial MCDF integro-differential equations for the radial orbitals are solved by numerical iteration [33].

3.1 Calculations using GRASP

We use the GRASP (General-Purpose Relativistic Atomic Structure Program) in two different implementations [33,34]. After the application of the MCDF method to solve the correlated relativistic Coulomb problem, the long-wavelength ($\omega \to 0$) Breit interaction correction is included by a CI method. Matrix elements of the Breit interaction operator

$$V^{\rm B}(0) = -\frac{e^2}{4\pi\varepsilon_0 r_{12}} \left[\vec{\alpha}_1 \cdot \vec{\alpha}_2 + \frac{(\vec{\alpha}_1 \cdot \vec{r}_{12})(\vec{\alpha}_2 \cdot \vec{r}_{12})}{r_{12}^2}\right] \qquad (12)$$

(Eq. 3 for $\omega \to 0$) are calculated with wave functions generated by the Coulomb self-consistent method and added to the Dirac–Coulomb Hamiltonian matrix. The resulting matrix is rediagonalized. The frequency-dependent part of the Breit interaction operator (Eq. 3) is evaluated by perturbation theory employing Dirac–Coulomb eigenfunctions. Approximate quantum electrodynamic corrections to level energies are evaluated as described in Ref. [34].

The wave function of the recombining initially free electron with an asymptotic three-momentum $\vec{p}$ and spin projection m_s is represented by a partial wave expansion [35],

$$|E\vec{p}m_s\rangle = \sum_{\kappa m} i^l e^{i\Delta_\kappa} \sum_{m_l} Y^*_{lm_l}(\hat{r}) \times C\left(l\ \frac{1}{2}\ m_l\ m_s; j\ m\right) |E\kappa m\rangle . \qquad (13)$$

The phases Δ_κ are chosen such that the continuum wave function fulfills the boundary conditions of an incoming plane wave and an outgoing spherical wave. $Y_{lm_l}(\hat{r})$ is a spherical harmonic and the $C\left(l\ \frac{1}{2}\ m_l\ m_s; j\ m\right)$ stand for the vector coupling coefficients. The partial wave functions are represented in the spherical bispinor form similar to the bound orbitals in Eq. (11).

The DC rate, $A^{\mathrm{DC}}_{i\to d}$ is related to the Auger rate $A^{\mathrm{a}}_{i\to d}$ by the principle of detailed balance:

$$A^{\mathrm{DC}}_{i\to d} = \frac{2J_d+1}{2(2J_i+1)} A^{\mathrm{a}}_{i\to d}\,. \tag{14}$$

Here, J_d and $J_i = \frac{1}{2}$ are the total angular momenta of the intermediate and the initial states of the recombination process, respectively. The calculation of the Auger rate involves the evaluation of the matrix element of the Coulomb and Breit interactions between the initial bound-free product state and the doubly excited state d as detailed in Refs. [36–38].

3.2 Calculations using JAC

An independent set of MCDF computations have been carried out by using JAC, the Jena Atomic Calculator [39,40]. This code applies the MCDF method for the computation of atomic energy levels and wave functions as required for the evaluation of DR resonance energies, widths and strengths [41,42]. For the present computations of KLL DR cross sections of hydrogenlike Xe^{53+} ions, we used three different approaches with increasing level of detail. In the first approach, only the Coulomb interaction was considered in the evaluation of the transition energies and Auger rates that contribute to the resonance widths and strengths. In the second approach, the Breit interaction was taken into account in addition, by using the low-frequency limit of the Breit operator (Eq. 12). In the third approach, we additionally accounted for QED effects. These (so-called) radiative corrections can be incorporated into the level structure and transition matrix elements by means of a local single-electron QED Hamiltonian [43] that can be separated into two parts: the self-energy (SE) and vacuum polarization (VP). For multiply and highly charged ions, these two parts are usually comparable with each other but contribute with different sign. Since the QED formalism is the fundament of all atomic behavior, its predictions need to be verified under quite different conditions in order to understand the limits of standard atomic structure computations. However, explicit (non-local) calculations of these radiative corrections are time-consuming and still a challenge for many-electron systems, if the standard QED perturbation theory is to be applied.

4 Results

An overview over our experimental and theoretical results is provided by Fig. 1. On the scale of the figure, differences between our two theoretical approaches cannot be discerned. The experimental electron-ion collision-energy range 20.5−21.7 keV comprises all KLL DR resonances of the initially hydrogenlike Xe^{53+}.

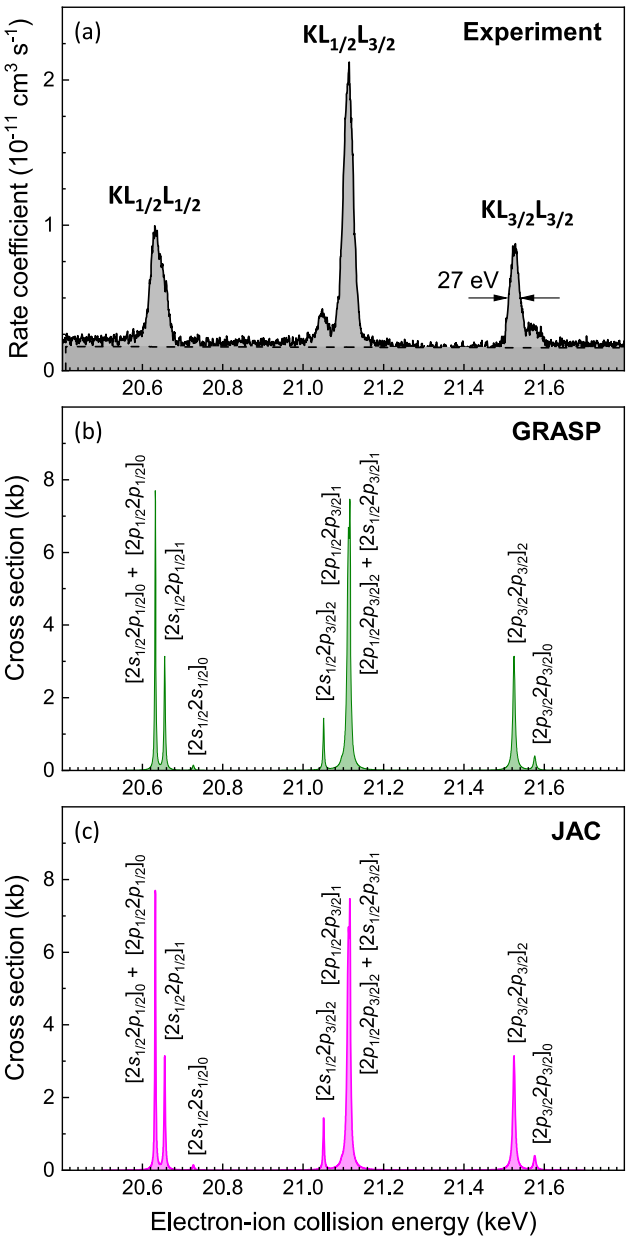

Fig. 1 **a** Measured recombination rate coefficients (solid line) and calculated rate coefficient for radiative recombination (RR, dashed line) for hydrogenlike xenon. **b**, **c** KLL DR cross sections from present GRASP and JAC results as provided in Table 1

Table 1 Calculated KLL DR resonance energies (E_r), resonance strengths (S) and natural line widths (Γ) and experimental resonance strengths for hydrogenlike Xe. The subscripts behind the closing brackets of the resonance designations are the values of the pertaining total angular momentum J. The GRASP (JAC) results were obtained with including QED effects and the frequency-dependent (independent) Breit interaction. The experimental uncertainty corresponds to the ±13% systematic uncertainty of the experimental rate coefficient. The tabulated resonance parameters were used for the cross-section plots in Fig. 1b and c as well as in the comparisons between experiment and theory as shown in Figs. 3c, 4c for GRASP and Figs. 3f, 4f for JAC

		GRASP			JAC			Experiment
No.	Resonance	E_r (eV)	S (kb eV)	Γ (eV)	E_r (eV)	S (kb eV)	Γ (eV)	S (kb eV)
	$\boldsymbol{KL_{1/2}L_{1/2}}$		**49.06**			**47.25**		**52.1±6.8**
1	$[2p_{1/2}^2]_0$	20632	22.80	2.23	20627	21.81	1.92	
2	$[2s_{1/2}2p_{1/2}]_0$	20632	7.60	3.60	20630	7.46	3.44	
3	$[2s_{1/2}2p_{1/2}]_1$	20656	17.50	3.57	20654	17.20	2.85	
4	$[2s_{1/2}^2]_0$	20727	1.16	5.13	20725	0.78	5.11	
	$\boldsymbol{KL_{1/2}L_{3/2}}$		**99.01**			**97.24**		**90.1±11.7**
5	$[2s_{1/2}2p_{3/2}]_2$	21051	7.36	3.31	21050	7.46	3.18	
6	$[2p_{1/2}2p_{3/2}]_1$	21096	1.05	6.80	21096	1.01	6.97	
7	$[2p_{1/2}2p_{3/2}]_2$	21112	64.40	6.94	21113	63.78	7.88	
8	$[2s_{1/2}2p_{3/2}]_1$	21116	26.20	3.39	21115	24.99	1.67	
	$\boldsymbol{KL_{3/2}L_{3/2}}$		**36.84**			**36.61**		**36.1±4.7**
9	$[2p_{3/2}^2]_2$	21525	32.80	6.65	21524	32.59	8.38	
10	$[2p_{3/2}^2]_0$	21576	4.04	6.60	21576	4.02	6.33	

Bold is the sum of the respective light entries thereunder

The experimental spectrum resolves three groups of $KL_{1/2}L_{1/2}$, $KL_{1/2}L_{3/2}$, and $KL_{3/2}L_{3/2}$ resonances associated with the $2\ell_j 2\ell'_{j'}$ configurations of the doubly excited intermediate heliumlike energy levels in the recombined Xe^{52+} ion with the two L-shell electrons having orbital angular momenta ℓ, ℓ' and total angular momenta $j, j' = 1/2$ or $3/2$. According to our theoretical calculations (see Table 1), the $KL_{1/2}L_{1/2}$, $KL_{1/2}L_{3/2}$, and $KL_{3/2}L_{3/2}$ resonance groups comprise twice four and once two fine-structure components, respectively, corresponding to different values of the total angular momentum J that results from the jj coupling of the two L shell electrons. In some cases, the fine-structure splitting is larger than the natural line widths, such that the respective fine-structure components can, in principle, be observed separately as suggested in Fig. 1.

The experimental energy spread δE is close to the natural line widths (for numerical values, see Table 1). In the case of the $KL_{1/2}L_{3/2}$ and the $KL_{3/2}L_{3/2}$ resonance groups, all theoretically separated fine-structure components are resolved also individually in the experimental data. For the $KL_{1/2}L_{1/2}$ group the splitting of the two main peaks is not fully resolved, but an according line asymmetry is apparent in the measured spectrum. The experimental energy spread can be inferred from the measured resonance peak of the isolated $[2p_{3/2}2p_{3/2}]_2$ resonance at the resonance energy $E_r \approx 21.5$ keV. The experimental FWHM of this peak is 27 eV (Fig. 1a). From this, we infer $\delta E = 26$ eV when considering also the theoretical width $\Gamma \approx 8$ eV of this resonance (Table 1). Thus, the relative experimental energy spread in our collision spectroscopy experimental approach amounts to 1.2×10^{-3}. This is almost a factor of two better than the experimental resolution that was obtained in the above mentioned EBIT experiments [10].

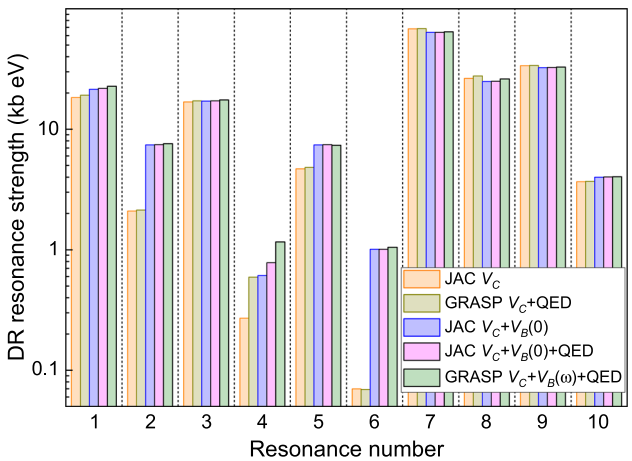

Fig. 2 Calculated KLL DR resonance strengths for hydrogenlike Xe using various approaches for the calculation of Auger rates and radiative rates. See Table 1 for the assignments of the resonance numbers on the abscissa

Different calculations have been performed to access and understand the impact of the Breit interaction and of QED contributions on the computed resonance strengths by stepwise incorporating these effects. Figure 2 compares the resonance strengths, which are most sensitive to the Breit interaction with the $KL_{1/2}L_{1/2}$ $[2s_{1/2}2p_{1/2}]_0$ (No. 2 in Fig. 2 and Table 1) resonance being affected particularly strongly. Its strength increases by a factor of 3.5. The strength of the

$KL_{1/2}L_{3/2}$ $[2s_{1/2}2p_{3/2}]_1$ (No. 6) resonance increases by an even larger factor of 15, but this resonance is comparatively weak. In general, QED effects alter the resonance strengths on a (sub)percent level with the exception of the comparatively weak $KL_{1/2}L_{1/2}$ $[2s_{1/2}2s_{1/2}]_0$ resonance (No. 4) which increases in strength by 28% upon the inclusion of QED effects in addition to the Breit interaction due to a modified configuration mixing.

When both the Breit interaction and QED effects are included, the calculated resonance strengths from both our theoretical approaches agree within 1–5 percent (Table 1), except for the weakest resonance, i.e., the $[2p_{1/2}2p_{1/2}]_0$ resonance, where the difference between both theoretical approaches is considerably larger. The relative differences are somewhat larger for the computed resonance widths and may be partly due to the neglect of the frequency-dependent part of the Breit interaction in the JAC calculations. The agreement between the two approaches is best for the resonance positions which generally differ by no more than 2 eV, again except for the weak $[2p_{1/2}2p_{1/2}]_0$ resonance, where the GRASP and JAC resonance energies differ by 5 eV. Table 1 also provides the experimental integrated resonance strengths for the $KL_{1/2}L_{1/2}$, $KL_{1/2}L_{3/2}$, and $KL_{3/2}L_{3/2}$ resonance groups. Within their ±13% systematic uncertainty, all of these agree with the theoretical findings if the Breit interaction and QED effects are considered in the theoretical calculations.

For a visual comparison of the experimental merged-beams rate coefficients with the theoretical cross sections, the latter have been convolved with the experimental collision-energy distribution using a Monte Carlo approach which is described in Appendix B. The simulated experimental response function includes contributions from the electron and ion beam energy spreads, from the finite drift tube length and associated fringe-field effects, and from angular variations of the guiding magnetic field of the ESR electron cooler. In addition to DR, also radiative recombination (RR) was considered by using a semiclassical cross-section formula, which yielded excellent agreement with measured RR rate coefficients for heavy bare ions [30,44], when the cut-off due to field ionization in the storage-ring dipole magnet was accounted for. For the present experimental conditions, the maximum quantum number, that is not field ionized, is estimated to be $n_{\max} = 80$. In the Monte Carlo simulation, the DR and RR contributions are added incoherently, thus neglecting any possible quantum-mechanical interference between these two processes. Such interference effects were theoretically predicted for KLL DR of highly charged uranium ions [37,45] but not detected in our previous experiment with H-like U^{91+} [25]. Observations of this effect have been reported, e.g., in Refs. [46–49].

Figures 3, 4 display the comparisons of measured and simulated recombination rate coefficients for hydrogenlike xenon. The latter are based on our five different theoretical approaches, i.e., 'GRASP Coulomb+QED' (Figs. 3b, 4b), 'GRASP Coulomb+Breit(ω>0)+QED' (Figs. 3c, 4c), 'JAC Coulomb' (Figs. 3d, 4d), 'JAC Coulomb+Breit(ω=0)' (Figs. 3e, 4e), and 'JAC Coulomb+Breit(ω=0)+QED' (Figs. 3f, 4f). The experimental data are the same in all panels. When QED effects are neglected, the simulated spectra have to be shifted by 39 eV toward lower energies in order to line up the simulated resonance structures with the experimental ones (Fig. 3d, e). This shift is larger than the ±16 eV uncertainty of the experimental energy scale.

A clear signature of the Breit interaction on the strength of the $KL_{1/2}L_{1/2}$ group of DR resonances can be seen when comparing Fig. 4b, d on the one hand and Fig. 4c, e on the other hand. When the Breit interaction is neglected, the strength of the $KL_{1/2}L_{1/2}$ group of DR resonances is underestimated significantly. In both our theoretical approaches, the Breit interaction increases the theoretical $KL_{1/2}L_{1/2}$ resonance strength by 25%. The present findings are qualitatively the same as for KLL DR of hydrogenlike uranium, where satisfying agreement between experiment and 'Coulomb+Breit' theory was found [25]. There the Breit interaction increased the $KL_{1/2}L_{1/2}$ resonance strength by 44%. As expected from the Z^4 scaling of the Breit contribution to the Auger rates [5] and as found previously for DR of lithiumlike ions [10], the contribution of the Breit interaction decreases with decreasing nuclear charge Z also for DR of hydrogenlike ions. An excellent agreement between experiment and simulations can only be achieved when Breit interaction and QED are both taken into account. Then, the GRASP calculations (Figs. 3c, 4c) provide an overall slightly better agreement with the experimental data than the JAC calculations (Figs. 3f, 4f), which neglect the frequency-dependent part of the Breit interaction. No attempt has been made so far to incorporate into JAC the frequency-dependent Breit interaction explicitly, which is known to be negligible in (almost) all observables for light and medium-Z elements. The frequency dependence in the electron–electron interaction can be only derived in a QED framework, i.e., assuming that the electromagnetic interaction is indeed mediated by a photon of finite frequency, while the frequency-independent Breit operator can also be derived classically [50].

5 Summary and conclusions

In summary, we have measured the absolute KLL dielectronic recombination rate coefficient of hydrogenlike xenon by high-resolution electron-collision spectroscopy. In the experimental energy range, our experimental resolving power is competitive with that in EBIT experiments. As the conceptually simplest atomic systems, hydrogenlike ions and their collision processes can be theoretically treated with the highest precision.

Our experimental data and our theoretical results from two independent multi-configuration Dirac–Fock calculations are in excellent mutual agreement, if the latter account for QED effects and the Breit interac-

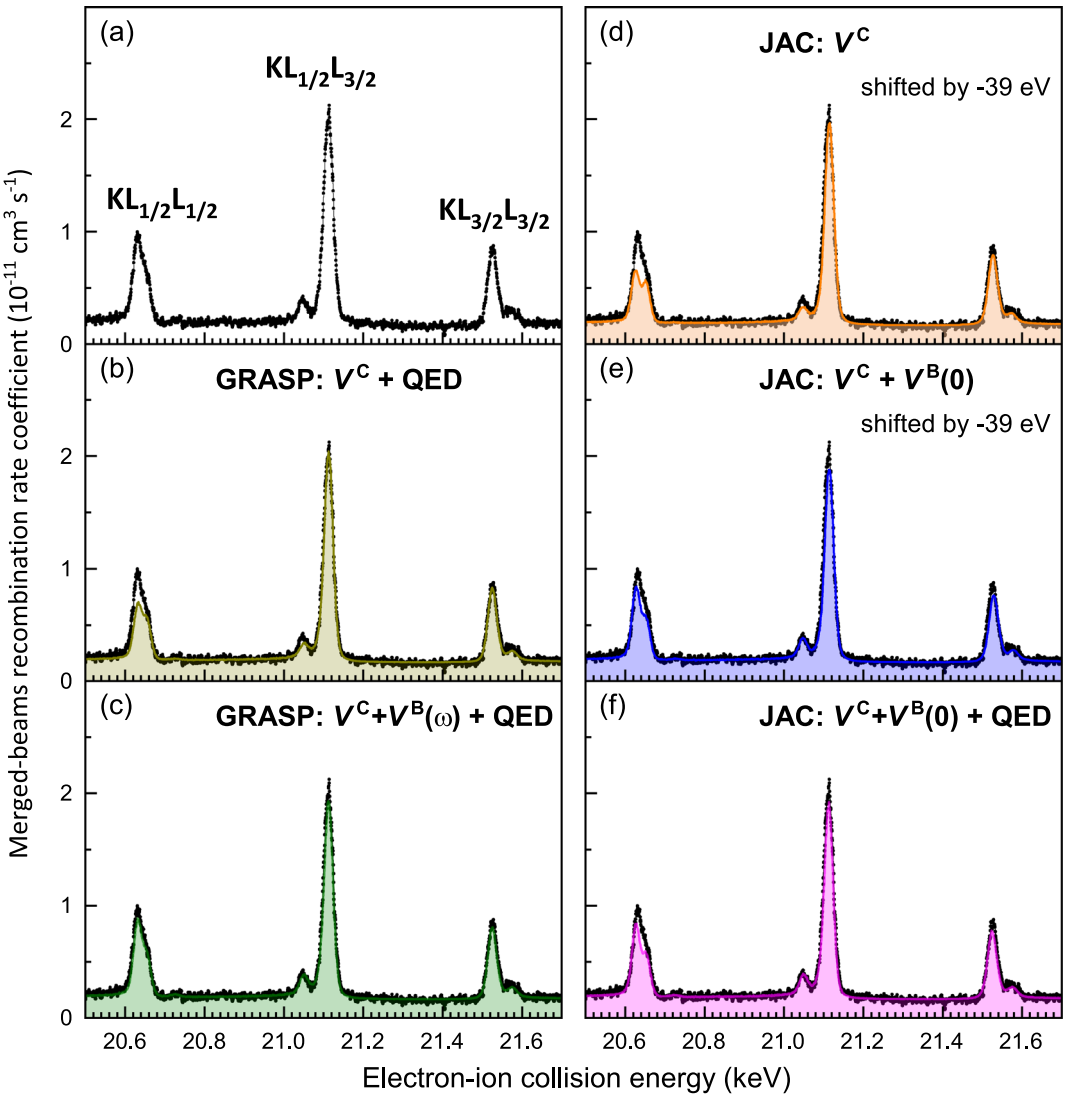

Fig. 3 Comparison between the experimental (symbols, panels **a**–**f**) and Monte Carlo simulated recombination rate coefficients (solid and shaded lines) based on the results from the present GRASP (panels **b**, **c**) and JAC (panels **d**, **e**, **f**) calculations. Note that the JAC results without QED in panels (**d**) and (**e**) had to be shifted by −39 eV (toward lower energies) in order to line up the theoretical with the experimental resonance positions

tion. As already found in previous work [10,25] not all DR resonance strengths are affected by the Breit interaction in the same way. A significant 25% increase was found for the strength of the $KL_{1/2}L_{1/2}$ resonance group, largely owing to a factor of three increase in strength of only one of the four members of this group. This confirms earlier findings for DR of H-like U^{91+}, where the Breit interaction was found to contribute by 40% to the $KL_{1/2}L_{1/2}$ DR resonance strength [25]. The decrease in its influence with decreasing nuclear charge is according to the expectations [5].

A further increase in the experimental resolving power in electron-ion collision spectroscopy is conceivable, in particular, at the low-energy heavy-ion storage CRYRING, which recently has been moved from its original location at Stockholm, Sweden, to the international Facility for Ion and Antiproton Research (FAIR) on the premises of GSI [51]. Commissioning experiments [52] have already confirmed that the ultracold electron beam of the CRYRING electron cooler provides a much lower electron energy spread than its counter-part at the ESR. Under these conditions, even a measurement of the natural line widths of *KLL* DR resonances in highly charged heavy ions is expected to become feasible.

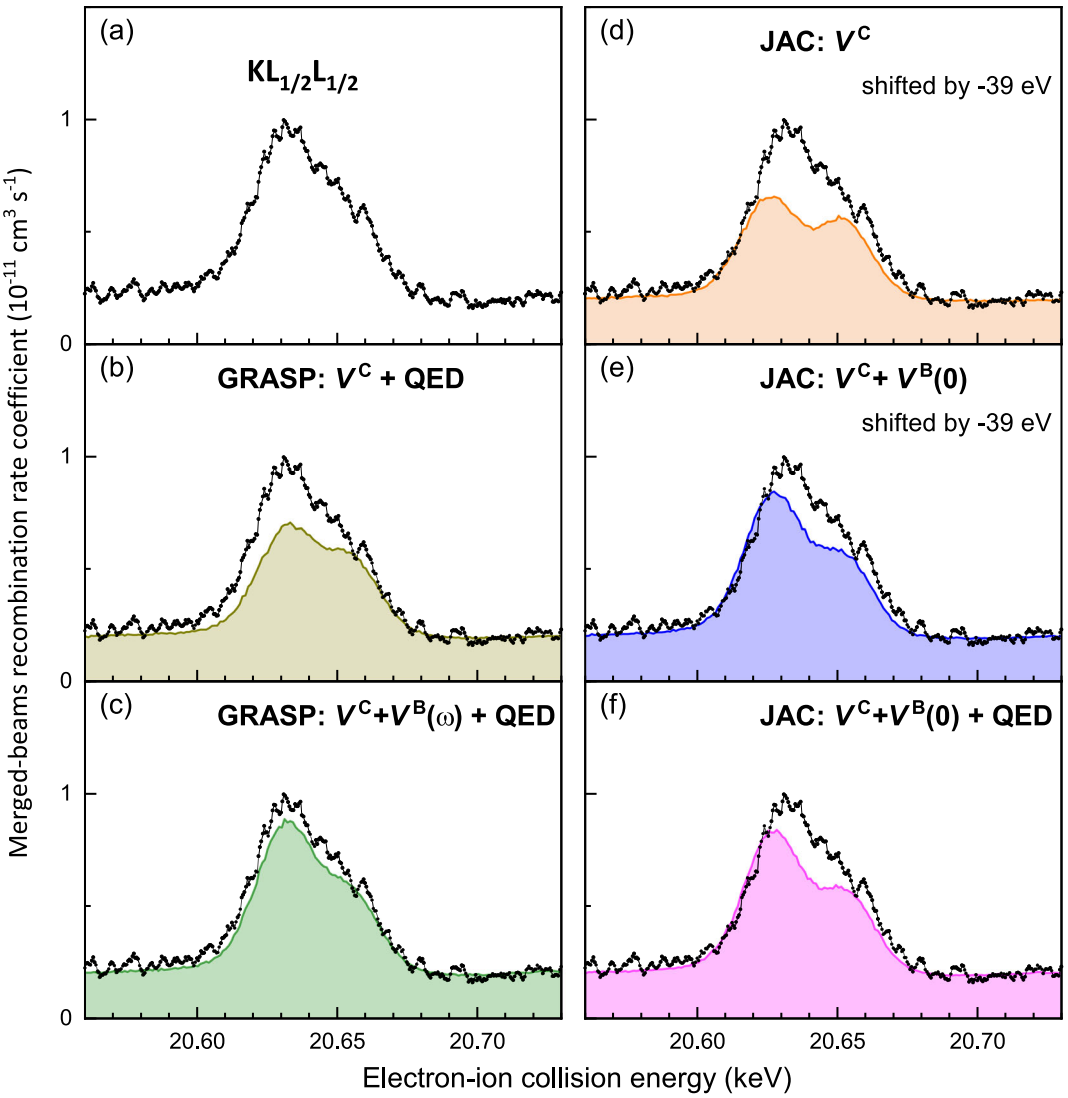

Fig. 4 Same as Fig. 3, but zoomed in on the $KL_{1/2}L_{1/2}$ resonance group

Acknowledgements We dedicate this publication to our late colleagues Dr. Peter Beller and Dr. Fritz Nolden. Their contributions in particular to the stochastic cooling method were decisive for the success of the present experiment. The present results have been obtained in the frame of the FAIR Phase-0 research program at GSI, Darmstadt (Germany). We thankfully acknowledge the contributions by K. Beckert, S. Böhm, F. Bosch, B. Franzke, N. Grün, J. Jacobi, S. Kieslich, H. Knopp, P. Mokler, W. Scheid, W. Shi, and Z. Stachura to the early stage of the project. Financial support by the German Ministry for Education and Research (BMBF) via grant no. 06 GI 947, via the GSI University Collaborative Research Programme (grant nos. GSI MÜ1 and GSI MÜ2), and via the Collaborative Research Center APPA (ErUM-FSP T05, grant nos. 05P21RGFA1 and 05P21SJFAA) is gratefully acknowledged. We thank the Deutsche Forschungsgemeinschaft for support via grant no. 5258018. S.-X.W. and C.B. acknowledge the support by the State of Hesse within the Research Cluster ELEMENTS (Project ID 500/10.006).

Author contributions

C.K. and A.M. proposed the experiment. C.B., C.K., A.M., M.S., and S.S. performed the experiment. C.B., S.F., S.S., and S.-X.W. analyzed the data. St.F., Z.H., and W.S. performed the atomic calculations. S.-X.W. and S.S. wrote the first draft of the paper. All authors contributed equally to the final version of the manuscript.

Funding Information Open Access funding enabled and organized by Projekt DEAL.

Data Availability Statement This manuscript has associated data in a data repository. [Authors' comment: The data will be made available by the corresponding author on reasonable requests.]

Appendix A Experimental merged-beams rate coefficient

Here, we provide the derivation of Eq. 4, which was first introduced in Ref. [25].

In collision experiments, the number of detector counts N per unit interaction volume V and per unit time τ is related to the respective cross-section σ via

$$\frac{N}{V\tau} = \sigma\mathcal{L} \tag{A1}$$

were the Luminosity density $\mathcal{L}$ characterizes the experiment. Since σ, N, and the space-time volume $V\tau$ are Lorentz invariant also $\mathcal{L}$ must be so. When expressed in terms of the number densities n_e and n_i and velocities $\vec{\beta}_e$ and $\vec{\beta}_i$ of the electrons and the ions, respectively, the Lorentz invariant expression of the luminosity density is [53,54]

$$\mathcal{L} = n_e n_i \left(1 - \vec{\beta}_e \cdot \vec{\beta}_i\right) v_{\mathrm{rel}}, \tag{A2}$$

where

$$\frac{v_{\mathrm{rel}}}{c} = \beta_{\mathrm{rel}} = \frac{\sqrt{\left(\vec{\beta}_e - \vec{\beta}_i\right)^2 - \left(\vec{\beta}_e \times \vec{\beta}_i\right)^2}}{1 - \vec{\beta}_e \cdot \vec{\beta}_i} \tag{A3}$$

is the Lorentz invariant expression for the relative velocity [50,54]. It can be easily shown that

$$\gamma_{\mathrm{rel}} = \frac{1}{\sqrt{1-\beta_{\mathrm{rel}}^2}} = (1 - \vec{\beta}_e \cdot \vec{\beta}_i)\gamma_e\gamma_i \tag{A4}$$

is identical to Eq. 6.

For collinear beams, i.e., for $\vec{\beta}_e \| \vec{\beta}_i$, Eq. A3 reduces to the well-known expression

$$v_{\mathrm{rel}} = \frac{|v_e - v_i|}{1 - \beta_e\beta_i}, \tag{A5}$$

and Eq. A2 becomes

$$\mathcal{L} = n_e n_i v_{\mathrm{rel}} \left(1 - \beta_e\beta_i\right) = n_e n_i |v_e - v_i|. \tag{A6}$$

Insertion into Eq. A1 and integration over the volume V results in the reaction rate

$$R = \frac{N}{\tau} = \sigma \int_V v_{\mathrm{rel}} \left(1 - \beta_e\beta_i\right) n_e n_i dV. \tag{A7}$$

In the merged-beams arrangement, all quantities that appear in the integrand are independent of the spatial coordinates such that the volume integration just provides a factor $V = AL$ with A and L being the geometrical cross section of the ion beam and the length of the interaction region, respectively. After additionally introducing the rate coefficient

$$\alpha_{\mathrm{mb}} = \langle \sigma v_{\mathrm{rel}} \rangle, \tag{A8}$$

the reaction rate can be expressed at

$$\begin{aligned} R &= \alpha_{\mathrm{mb}} \left(1 - \beta_e\beta_i\right) n_e n_i \, AL \\ &= \alpha_{\mathrm{mb}} \left(1 - \beta_e\beta_i\right) n_e N_i \, L/C, \end{aligned} \tag{A9}$$

where in the last step the ion density $n_i = N_i/(AC)$ has as usual been expressed in terms of the number N_i of stored ions and the circumference C of the ion orbit in the storage ring. A simple rearrangement of Eq. A9 finally yields the experimental merged-beams rate coefficient:

$$\alpha_{\mathrm{mb}} = \frac{R_{\mathrm{exp}} C}{\eta \left(1 - \beta_e\beta_i\right) n_e N_i L}, \tag{A10}$$

where the experimental reaction rate $R_{\mathrm{exp}} = R\eta$ accounts for the detection efficiency η. Equation A10 is identical with Eq. 4.

For small differences between electron and ion velocity, i.e., for $\beta_e \approx \beta_i$, one obtains $(1 - \beta_e\beta_i)^{-1} \approx (1 - \beta_i\beta_i)^{-1} = \gamma_i^2$, and Eq. 4 becomes

$$\alpha_{\mathrm{mb}} \approx \frac{R_{\mathrm{exp}} C \gamma_i^2}{\eta n_e N_i L}. \tag{A11}$$

This approximation is frequently encountered in the literature. As pointed out already earlier [21], it leads to significant errors if the electron and ion velocity differ by more than a few percent as was the case in Ref. [25] and is here as well.

Appendix B Merged-beams rate coefficient from theoretical cross section

For the comparison of experimental merged-beams rate coefficients (Eq. 4) with theoretical cross sections, the

latter have to be convolved with the experimental distribution of relative velocities between ions and electrons. In an electron cooler, the velocity distribution of the electron beam is anisotropic and characterized by different beam temperatures $T_\parallel$ and $T_\perp$ in the beam direction and perpendicular to the beam direction, respectively. Since $T_\parallel < T_\perp$, it is referred to as 'flattened Maxwellian' [28]

$$f(\vec{v}, v_e)\, d^3\vec{v} = \left(\frac{m_e}{2\pi k}\right)^{3/2} \frac{1}{T_\parallel^{1/2} T_\perp} \exp\left(-\frac{m_e(v_\parallel - v_e)^2}{2kT_\parallel} - \frac{m_e v_\perp^2}{2kT_\perp}\right) v_\perp dv_\perp dv_\parallel d\varphi, \quad \text{(B12)}$$

where the velocity components $v_\parallel$ and $v_\perp$ and the angle φ form a cylindrical coordinate system and where v_e denotes the mean electron beam velocity in the laboratory frame. As usual, m_e and k are the electron rest mass and Boltzmann's constant, respectively.

If one neglects the velocity spread of the ions and assumes that all ions move with velocity v_i (in the laboratory frame) in the electron beam direction, the theoretical merged-beams rate coefficient can be calculated from the cross-section $\sigma(v)$ as

$$\alpha_{\mathrm{mb}}(v_{\mathrm{rel}}) = \langle \sigma v_{\mathrm{rel}} \rangle = \int_0^\infty v_\parallel \sigma(v_\parallel) f(\vec{v}, v_{\mathrm{rel}}) d^3\vec{v}. \quad \text{(B13)}$$

with v_{rel} from Eq. A5. Since the cross section does not depend on $v_\perp$ and φ, the integrations over these variables can be carried out assuming nonrelativistic kinematics

$$\alpha_{\mathrm{mb}}(E_{\mathrm{cm}}) = \int_0^\infty \sqrt{\frac{2E}{m_e}}\, \sigma(E)\, f(E, E_{\mathrm{cm}})\, dE\,, \quad \text{(B14)}$$

with $E_{\mathrm{rel}} = E_{\mathrm{cm}}$ from Eq. 5, $E = \frac{1}{2} m_e v_\parallel^2$, and

$$f(E, E_{\mathrm{cm}}) = \frac{1}{2kT_\perp \xi} \exp\left(-\frac{E - E_{\mathrm{cm}}/\xi^2}{kT_\perp}\right) \times \left[\mathrm{erf}\left(\frac{\sqrt{E} + \sqrt{E_{\mathrm{cm}}/\xi^2}}{\sqrt{kT_\parallel}/\xi}\right) + \mathrm{erf}\left(\frac{\sqrt{E} - \sqrt{E_{\mathrm{cm}}/\xi^2}}{\sqrt{kT_\parallel}/\xi}\right)\right] \quad \text{(B15)}$$

with $\xi = \sqrt{1 - T_\parallel/T_\perp}$.

For a delta-like sharp resonance with strength S_{DR} and resonance energy E_r, the cross section is

$$\sigma(E) = S_{\mathrm{DR}} \delta(E_r - E) \quad \text{(B16)}$$

and one obtains from Eqs. B14 and B15

$$\alpha_{\mathrm{mb}}(E_{\mathrm{cm}}) = \frac{S_{\mathrm{DR}}}{kT_\perp \xi} \sqrt{\frac{E_r}{2m_e}} \exp\left(-\frac{E_r - E_{\mathrm{cm}}/\xi^2}{kT_\perp}\right) \times \left[\mathrm{erf}\left(\frac{\sqrt{E_r} + \sqrt{E_{\mathrm{cm}}/\xi^2}}{\sqrt{kT_\parallel}/\xi}\right) + \mathrm{erf}\left(\frac{\sqrt{E_r} - \sqrt{E_{\mathrm{cm}}/\xi^2}}{\sqrt{kT_\parallel}/\xi}\right)\right]. \quad \text{(B17)}$$

Equation B17 is a good representation of the DR merged-beams rate coefficient for resonances with intrinsic widths much smaller than the experimental energy spread [55]

$$\Delta E = \sqrt{(kT_\perp \ln 2)^2 + 16 \ln 2\, kT_\parallel E_{\mathrm{rel}}}. \quad \text{(B18)}$$

For broader resonances with Lorentzian or other line shapes, the integral in Eq. B14 has to be computed numerically [56,57].

A more fundamental limitation of Eqs. B14 and B17 is that the underlying velocity distribution (Eq. B12) is nonrelativistic. However, relativistic effects must be expected for large relative velocities in Eq. B13. In principle, one could start from a relativistic generalization [58] of Eq. B12, which would anyhow require a numerical treatment of the calculation of recombination rate coefficients. Instead, we use a Monte Carlo approach for deriving the collision-energy distribution which allows one to account not only for relativistic, but also flexibly for instrumental effects as discussed in the following.

In the merging and demerging regions of an electron cooler, the electron beam is bent onto and away from the ion beam by toroidal magnetic fields. Recombination events in these sections, where the velocity vectors $\vec{v_i}$ and $\vec{v_e}$ are not pointing into the same direction, lead to a slight broadening of the observed resonances. This (small) effect can be accounted for, e.g., by deconvolving the experimental data [59], such that it does not need to be considered anymore in the calculation of merged-beams rate coefficients from theoretical DR cross sections. Here, we include the merging and demerging effects in our Monte Carlo approach (see below).

Some electron coolers, e.g., the ones at the ESR [60,61] and CSR [62,63] storage rings are equipped with drift tubes which allow for controlling the electron-ion collision energy by setting the drift tube voltage U_{dt} to the desired value (Eq. 7). The drift tubes surround the particle beams in the straight sections of the electron coolers. Their finite length L_{dt} leads to fringe-field effects and, thus, to a dependence of U_{dt} on the coordinate z along the cooler axis. For a cylindrical tube with radius r_{dt}, the on-axis potential can be approximated as [61,64]

$$\frac{U_{\mathrm{dt}}(z)}{U_{\mathrm{dt}}(0)} = \frac{1}{2} + \frac{1}{2} \tanh\left(1.318 \frac{L_{\mathrm{dt}}/2 - |z|}{r_{\mathrm{dt}}}\right), \quad \text{(B19)}$$

where $U_{\mathrm{dt}}(0)$ denotes the voltage, that is applied to the drift tube, and where $z = 0$ is in the middle of drift tube. The z dependence of the drift tube potential leads (via Eqs. 5–7) to a z dependence of the electron energy

which has to be accounted for in the calculation of the merged-beams rate coefficient.

At the ESR, another z-dependent effect comes from inhomogeneities of the magnetic field $\vec{B}$ which is generated by a solenoid and guides the electrons through the electron cooler. The light electrons follow the magnetic field lines while the heavier ions are not affected. Due to mechanical imperfections, the direction of $\vec{B}$ locally deviates slightly from the ion beam direction. This introduces nonzero angles $\theta(z)$ in the yz-plane between electron velocity $\vec{v}_e$ and ion velocity $\vec{v}_i$ which locally also affects the electron-ion collision energy (Eq. 5). For the ESR storage ring, the function $\theta(z)$ is plotted in Refs. [61,65]. It also accounts for the bending of the electron beam in the toroidal sections of the electron cooler discussed above. Accordingly, $\theta > 0$ along the entire cooler length. In an experiment, the beams are usually optimized such that they are aligned along the $\vec{B}$-field direction and not along the geometric cooler axis. This can be taken into account by subtracting an offset angle $\theta_0 = 0.48$ mrad from $\theta(z)$.

In order to account for the described effects and, in addition, for the velocity spread of the ions, we use a Monte Carlo approach for the calculation of the electron energy distribution function $f(E, E_{\mathrm{cm}})$. In this approach, the energy E along the cooler axis is subdivided into N energy bins $[E_n - \epsilon, E_n]$ of constant bin width ϵ with $E_n = E_0 + n\epsilon$ for $n = 1, \ldots, N$ and suitably chosen E_0.

For fixed ion energy E_i and for each nominal E_{cm}, the three components $\beta_{e,x}^{(G)}$, $\beta_{e,y}^{(G)}$ and $\beta_{e,z}^{(G)}$ of the randomly distributed laboratory electron velocity $\vec{\beta}_e^{(s)}$ are sampled from Gaussian distributions with the standard deviations $\sigma_{e,x} = \sigma_{e,y} = \sqrt{kT_\perp/m_e c^2}$ and $\sigma_{e,z} = \sqrt{kT_\parallel/m_e c^2}$ according to Eq. B12. Likewise, the three components $\beta_{i,x}^{(G)}$, $\beta_{i,y}^{(G)}$ and $\beta_{i,z}^{(G)}$ of the randomly distributed laboratory ion velocity $\vec{\beta}_i^{(s)}$ are sampled from normal distributions with $\sigma_{i,x} = \sigma_{i,y} = \sqrt{kT_{i\perp}/m_i c^2}$ and $\sigma_{i,z} = \delta\beta_i/\sqrt{8\ln 2}$, where T_i is the transverse ion temperature and $\delta\beta_i$ denotes the FWHM velocity spread of the ions in beam direction. Thus, sampled velocity components are modified by $U_{\mathrm{dt}}(z)$ and $\theta(z)$ which are both calculated for a z value that is drawn from a uniform distribution over the interval $[-L_t - L/2, L/2 + L_t]$ with L being the length of the electron cooler (Eq. 4). The additional sampling length L_t reaches into the toroidal sections of the cooler where the electron beam is bent onto and away from the ion beam.

From the sampled value $U_{\mathrm{dt}}(z)$, the associated gamma factor $\gamma_e(z)$ is readily calculated via Eq. 7 with the sum $-eU_{\mathrm{cath}} + eU_{\mathrm{sc}}$ obtained from E_{cm} and $\gamma_i = 1 + E_i/m_i c^2$ by inverting Eqs. 5 and 7 for $U_{\mathrm{dt}} = 0$. Taking also $\theta(z)$ into account, the sampled components of the laboratory electron velocity are

$$\begin{aligned}\beta_{e,x}^{(s)} &= \beta_{e,x}^{(G)},\\ \beta_{e,y}^{(s)} &= \beta_{e,y}^{(G)} + \beta_{e,\parallel}(z)\sin\left(\theta(z)\right),\end{aligned}$$

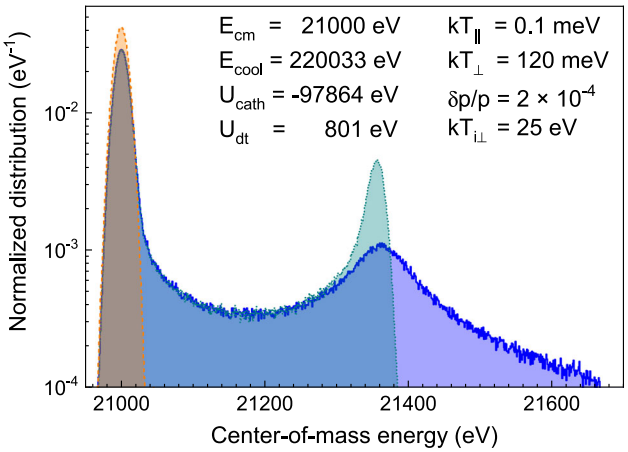

Fig. 5 Computed electron energy distributions $\tilde{f}/\epsilon$ for the ESR cooler. The dashed line was obtained for a scenario where the z-dependence of the drift tube potential and of the misalignment angle were not taken into account. The dotted and solid lines result when only the z-dependence of the drift tube potential is considered and when additionally the misalignment angle is accounted for, respectively. Some parameter values are supplied in the figure. The number of Monte Carlo iterations was 1000000 in each case

$$\beta_{e,z}^{(s)} = \beta_{e,z}^{(G)} + \beta_{e,\parallel}(z)\cos\left(\theta(z)\right) \tag{B20}$$

with $\beta_{e,\parallel}(z) = \sqrt{1 - [\gamma_e(z)]^{-2}}$. The ion energy is only slightly modified by the drift tube potential. With $\gamma_i(z) = 1 + [E_i - qeU_{\mathrm{dt}}(z)]/m_i c^2$ and $\beta_{i,\parallel}(z) = \sqrt{1 - [\gamma_i(z)]^{-2}}$, the sampled components of the laboratory ion velocity are

$$\begin{aligned}\beta_{i,x}^{(s)} &= \beta_{e,x}^{(G)},\\ \beta_{i,y}^{(s)} &= \beta_{e,y}^{(G)},\\ \beta_{i,z}^{(s)} &= \beta_{e,z}^{(G)} + \beta_{i,\parallel}(z).\end{aligned} \tag{B21}$$

With $\vec{\beta}_e^{(s)}$ and $\vec{\beta}_i^{(s)}$ specified, the "sampled" electron-ion collision energy $E_{\mathrm{cm}}^{(s)}$ in the center-of-mass frame can be calculated using $\vec{\beta}_e^{(s)} \cdot \vec{\beta}_i^{(s)} = \beta_e^{(s)}\beta_i^{(s)}\cos\theta$ in connection with Eqs. 6 and 5. Finally, the content of the energy bin which fulfills the condition $E_n - \epsilon \le E_{\mathrm{cm}}^{(s)} < E_n$ is incremented by 1.

A histogram $\tilde{f}(E_n, E_{\mathrm{cm}})$ that approximates $f(E, E_{\mathrm{cm}})\,dE$ is constructed by repeating the sampling and energy-computation sequence for a number (typically a few 10,000) of times. Figure 5 shows computed distribution functions for the parameters given. The joint influence of the z-dependent drift tube potential U_{dt} and of the z-dependent misalignment angle $\theta(z)$ on the distribution function is obvious. In Fig. 5, the quantity $E_{\mathrm{cool}} = (m_e/m_i)E_i$ quantifies the laboratory ion energy E_i. The relative longitudinal ion momentum spread $\delta p/p$ (FWHM), which is readily available from the experiment, is used for calculating $\delta\beta_i = (\delta p/p)\beta_i(1 - \beta_i^2)$ from $p = m_i\gamma_i c\beta_i$.

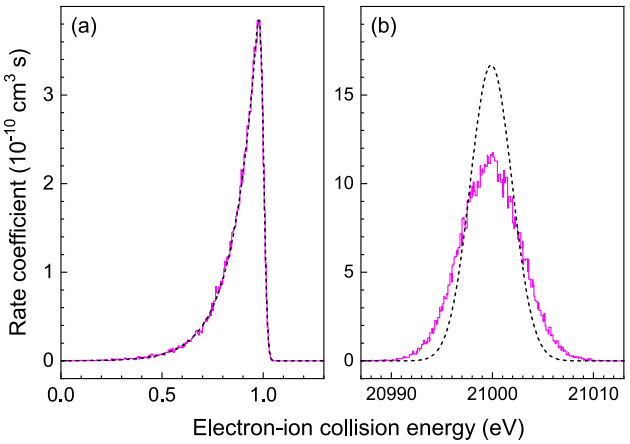

Fig. 6 Comparison of Monte Carlo results (magenta solid lines) for delta-like resonances with the nonrelativistic analytical formula (Eq. B17, black dashed lines). Panel (a) represents a nonrelativistic case with $E_r = 1$ eV, $E_{\rm cool} = 1000$ eV, $U_c = 978$ eV, and panel (b) a relativistic case with $E_r = 21000$ eV, $E_{\rm cool} = 220000$ eV, $U_c = 97800$ eV. In both cases, $S_{\rm DR} = 1$ Mb eV, $kT_{\parallel} = 0.1$ meV, $kT_{\perp} = 120$ meV, and $\delta p = 0$. In the Monte Carlo calculations, the drift tube fringe-field effects and the angular variations of the magnetic guiding field were disregarded. The excellent agreement between both curves in panel (a) validates our Monte Carlo code. In panel (b), the additional broadening due to the relativistic kinematics is apparent. The number of Monte Carlo iterations was 50,000 for each collision energy

Once the histogram $\tilde{f}(E_n, E_{\rm rel})$ is computed and properly normalized such that the sum over all energy bins yields 1, the merged-beams rate coefficient can be calculated as

$$\alpha_{\rm mb}(E_{\rm cm}) = \sum_{n=1}^{N} v_{\rm cm}(E_n)\overline{\sigma}(E_n)\tilde{f}(E_n, E_{\rm cm}), \quad \text{(B22)}$$

where (cf. Eq. A4)

$$v_{\rm cm}(E_n) = c\sqrt{1-\gamma_{\rm cm}^{-2}} \quad \text{(B23)}$$

with $\gamma_{\rm cm}$ obtained from inverting Eq. 5 for $E_{\rm cm} = E_n - \epsilon/2$ and

$$\overline{\sigma}(E_n) = \frac{1}{\epsilon}\int_{E_n-\epsilon}^{E_n} \sigma(E) \quad \text{(B24)}$$

is the cross section averaged over the n-th energy bin. For a Lorentzian line profile with intrinsic width Γ, i.e., for

$$\sigma(E) = \frac{S_{\rm DR}}{\pi}\frac{\Gamma/2}{(E-E_r)^2 + (\Gamma/2)^2}, \quad \text{(B25)}$$

the binned cross section can be computed analytically as

$$\overline{\sigma}(E_n) = \frac{S_{\rm DR}}{\pi\epsilon}\left[\text{atan}\left(\frac{E_n - E_r}{\Gamma}\right)\right.$$
$$\left. - \text{atan}\left(\frac{E_n - \epsilon - E_r}{\Gamma}\right)\right]. \quad \text{(B26)}$$

Table 2 Parameter values used in the Monte Carlo simulations that produced the theoretical rate coefficients shown in Fig. 3

Parameter (unit)	Value
Cooler length L (cm)	250
Additional sampling length L_t (cm)	2
Drift tube length $L_{\rm dt}$ (cm)	194
Offset angle θ_0 (mrad)	0.48
Cathode voltage $U_{\rm cath}$ (V)	−97864
Cooling energy $E_{\rm cool}$ (eV)	220033
Ion mass m_i (u)	135.907
Ion momentum spread $\delta p/p$	2×10^{-4}
Ion $kT_{i\perp}$ (eV)	25
Electron $kT_{\parallel}$ (meV)	0.1
Electron $kT_{\perp}$ (meV)	120
Monte Carlo iterations per $E_{\rm cm}$	20000

The accuracy of our Monte Carlo approach can be judged from Fig. 6a, where we compare the Monte Carlo result for a delta-like resonance under nonrelativistic conditions with the result of Eq. B17. The agreement is excellent. Figure 6b shows the results for a relativistic case and visualizes the limitations of the nonrelativistic derivation of merged-beams rate coefficients from theoretical cross sections. Finally, we mention that a different, less efficient Monte Carlo code had been in use earlier [65]. A comparison of the old code with the above described new code yielded identical results. Table 2 lists the parameter values that were used in the Monte Carlo simulations, the results of which are shown in Fig. 3.

References

1. J.A. Gaunt, R.H. Fowler IV., The triplets of helium. Phil. Transact. Roy. Soc. A **228**, 151 (1929). https://doi.org/10.1098/rsta.1929.0004
2. G. Breit, The effect of retardation on the interaction of two electrons. Phys. Rev. **34**, 553 (1929). https://doi.org/10.1103/PhysRev.34.553
3. J.B. Mann, W.R. Johnson, Breit interaction in multielectron atoms. Phys. Rev. A **4**, 41 (1971). https://doi.org/10.1103/PhysRevA.4.41
4. C.T. Chantler, T.V.B. Nguyen, J.A. Lowe, I.P. Grant, Convergence of the Breit interaction in self-consistent and configuration-interaction approaches. Phys. Rev. A **90**, 062504 (2014). https://doi.org/10.1103/PhysRevA.90.062504
5. P. Zimmerer, N. Grün, W. Scheid, Scaling of relativistic Auger rates with Z for ions with two electrons. J. Phys. B **24**, 2633 (1991). https://doi.org/10.1088/0953-4075/24/11/006
6. S. Fritzsche, G. Zschornack, G. Musiol, G. Soff, Interchannel interactions in highly energetic radiationless

transitions of neonlike ions. Phys. Rev. A **44**, 388 (1991). https://doi.org/10.1103/PhysRevA.44.388
7. N. Nakamura, Breit interaction effect on dielectronic recombination of heavy ions. J. Phys. B **49**, 212001 (2016). https://doi.org/10.1088/0953-4075/49/21/212001
8. T. Kandler, P.H. Mokler, T. Stöhlker, H. Geissel, H. Irnich, C. Kozhuharov, A. Kriessbach, M. Kucharski, G. Münzenberg, F. Nickel, P. Rymuza, C. Scheidenberger, Z. Stachura, T. Suzuki, A. Warczak, D. Dauvergne, R.W. Dunford, Transition selective investigation of the resonant transfer and excitation in $U^{90+} \rightarrow C$ collisions. Phys. Lett. A **204**, 274–280 (1995). https://doi.org/10.1016/0375-9601(95)00477-K
9. X. Ma, P.H. Mokler, F. Bosch, A. Gumberidze, C. Kozhuharov, D. Liesen, D. Sierpowski, Z. Stachura, T. Stohlker, A. Warczak, Electron-electron interaction studied in strong central fields by resonant transfer and excitation with H-like U ions. Phys. Rev. A **68**, 042712 (2003). https://doi.org/10.1103/PhysRevA.68.042712
10. N. Nakamura, A.P. Kavanagh, H. Watanabe, H.A. Sakaue, Y. Li, D. Kato, F.J. Currell, S. Ohtani, Evidence for strong Breit interaction in dielectronic recombination of highly charged heavy ions. Phys. Rev. Lett. **100**, 073203 (2008). https://doi.org/10.1103/PhysRevLett.100.073203
11. A. Gumberidze, D.B. Thorn, C.J. Fontes, B. Najjari, H.L. Zhang, A. Surzhykov, A. Voitkiv, S. Fritzsche, D. Banaś, H. Beyer, W. Chen, R.D. DuBois, S. Geyer, R.E. Grisenti, S. Hagmann, M. Hegewald, S. Hess, C. Kozhuharov, R. Märtin, I. Orban, N. Petridis, R. Reuschl, A. Simon, U. Spillmann, M. Trassinelli, S. Trotsenko, G. Weber, D.F.A. Winters, N. Winters, D. Yu, T. Stöhlker, Electron- and proton-impact excitation of hydrogenlike uranium in relativistic collisions. Phys. Rev. Lett. **110**, 213201 (2013). https://doi.org/10.1103/PhysRevLett.110.213201
12. Z. Hu, X. Han, Y. Li, D. Kato, X. Tong, N. Nakamura, Experimental demonstration of the Breit interaction which dominates the angular distribution of x-ray emission in dielectronic recombination. Phys. Rev. Lett. **108**, 073002 (2012). https://doi.org/10.1103/PhysRevLett.108.073002
13. Z. Hu, Y. Li, X. Han, D. Kato, X. Tong, H. Watanabe, N. Nakamura, Atomic-number dependence of the magnetic-sublevel population in the autoionization state formed in dielectronic recombination. Phys. Rev. A **90**, 062702 (2014). https://doi.org/10.1103/PhysRevA.90.062702
14. H. Jörg, Z. Hu, H. Bekker, M.A. Blessenohl, D. Hollain, S. Fritzsche, A. Surzhykov, J.R. Crespo López-Urrutia, S. Tashenov, Linear polarization of x-ray transitions due to dielectronic recombination in highly charged ions. Phys. Rev. A **91**, 042705 (2015). https://doi.org/10.1103/PhysRevA.91.042705
15. Z. Yang, J. Gao, W. Yan, K. Yao, J. Yang, Z. Wu, Z. Hu, Anisotropy and polarization of x-ray line emissions in the dielectronic recombination of hydrogenlike Fe^{25+} ions. Phys. Rev. A **104**, 022809 (2021). https://doi.org/10.1103/PhysRevA.104.022809
16. S. Fritzsche, A. Surzhykov, T. Stöhlker, Dominance of the Breit interaction in the x-ray emission of highly charged ions following dielectronic recombination. Phys. Rev. Lett. **103**, 113001 (2009). https://doi.org/10.1103/PhysRevA.103.113001
17. A. Müller, Electron-ion collisions: fundamental processes in the focus of applied research. Adv. At. Mol. Opt. Phys. **55**, 293 (2008). https://doi.org/10.1016/S1049-250X(07)55006-8
18. S. Schippers, Electron-ion merged-beam experiments at heavy-ion storage rings. Nucl. Instrum. Methods Phys. Res. B **350**, 61 (2015). https://doi.org/10.1016/j.nimb.2014.12.050
19. S. Schippers, T. Bartsch, C. Brandau, A. Müller, G. Gwinner, G. Wissler, M. Beutelspacher, M. Grieser, A. Wolf, R.A. Phaneuf, Dielectronic recombination of lithiumlike Ni^{25+} ions – high resolution rate coefficients and influence of external crossed E and B fields. Phys. Rev. A **62**, 022708 (2000). https://doi.org/10.1103/PhysRevA.62.022708
20. S. Böhm, S. Schippers, W. Shi, A. Müller, N. Djurić, G.H. Dunn, W. Zong, B. Jelenković, H. Danared, N. Eklöw, P. Glans, R. Schuch, Influence of electromagnetic fields on the dielectronic recombination of Ne^{7+} ions. Phys. Rev. A **64**, 032707 (2001). https://doi.org/10.1103/PhysRevA.64.032707
21. D. Bernhardt, C. Brandau, Z. Harman, C. Kozhuharov, S. Böhm, F. Bosch, S. Fritzsche, J. Jacobi, S. Kieslich, H. Knopp, F. Nolden, W. Shi, Z. Stachura, M. Steck, T. Stöhlker, S. Schippers, A. Müller, Spectroscopy of berylliumlike xenon ions using dielectronic recombination. J. Phys. B **48**, 144008 (2015). https://doi.org/10.1088/0953-4075/48/14/144008
22. S.X. Wang, Z.K. Huang, W.Q. Wen, W.L. Ma, H.B. Wang, S. Schippers, Z.W. Wu, Y.S. Kozhedub, M.Y. Kaygorodov, A.V. Volotka, K. Wang, C.Y. Zhang, C.Y. Chen, C. Liu, H.K. Huang, L. Shao, L.J. Mao, X.M. Ma, J. Li, M.T. Tang, K.M. Yan, Y.B. Zhou, Y.J. Yuan, J.C. Yang, S.F. Zhang, X. Ma, L.F. Zhu, Determination of the $2s^22p^5$ - $2s2p^6$ transition energy in fluorine-like nickel utilizing a low-lying dielectronic resonance. Phys. Rev. A **106**, 042808 (2022). https://doi.org/10.1103/PhysRevA.106.042808
23. F. Nolden, K. Beckert, P. Beller, B. Franzke, C. Peschke, M. Steck, Experience and prospects of stochastic cooling of radioactive beams at GSI. Nucl. Instrum. Methods Phys. Res. A **532**, 329 (2004). https://doi.org/10.1016/j.nima.2004.06.062
24. C. Brandau, C. Kozhuharov, A. Müller, S. Schippers, K. Beckert, P. Beller, D. Bernhardt, F. Bosch, S. Böhm, F.J. Currell, B. Franzke, A. Gumberidze, Z. Harman, J. Jacobi, P.H. Mokler, F. Nolden, W. Scheid, E.W. Schmidt, U. Spillman, Z. Stachura, M. Steck, T. Stöhlker, First dielectronic recombination measurements with H-like uranium. Radiat. Phys. Chem. **75**, 1763 (2006). https://doi.org/10.1016/j.radphyschem.2005.07.054
25. D. Bernhardt, C. Brandau, Z. Harman, C. Kozhuharov, A. Müller, W. Scheid, S. Schippers, E.W. Schmidt, D. Yu, A.N. Artemyev, I.I. Tupitsyn, S. Böhm, F. Bosch, F.J. Currell, B. Franzke, A. Gumberidze, J. Jacobi, P.H. Mokler, F. Nolden, U. Spillman, Z. Stachura, M. Steck, T. Stöhlker, Breit interaction in dielectronic recombination of hydrogenlike uranium. Phys. Rev. A **83**, 020701(R) (2011). https://doi.org/10.1103/PhysRevA.83.020701

26. A. Wolf, V. Balykin, W. Baumann, J. Berger, G. Bisoffi, P. Blatt, M. Blum, A. Faulstich, A. Friedrich, M. Gerhard, C. Geyer, M. Grieser, R. Grieser, D. Habs, H.W. Heyng, B. Hochadel, B. Holzer, G. Huber, E. Jaeschke, M. Jung, A. Karafillidis, G. Kilgus, R. Klein, D. Krämer, P. Krause, M. Krieg, T. Kühl, K. Matl, A. Müller, M. Music, R. Neumann, G. Neureither, W. Ott, W. Petrich, B. Povh, R. Repnow, S. Schröder, R. Schuch, D. Schwalm, P. Sigray, M. Steck, R. Stokstad, E. Szmola, M. Wagner, B. Wanner, K. Welti, S. Zwickler, First atomic physics experiments with cooled stored ion beams at the Heidelberg heavy-ion ring TSR. in AIP Conference Proceedings , vol .**205**, p. 378 (1990). https://doi.org/10.1063/1.39253
27. M. Steck, K. Beckert, H. Eickhoff, B. Franzke, F. Nolden, H. Reich, B. Schlitt, T. Winkler, Anomalous temperature reduction of electron-cooled heavy ion beams in the storage ring ESR. Phys. Rev. Lett. **77**, 3803 (1996). https://doi.org/10.1103/PhysRevLett.77.3803
28. H. Poth, Electron cooling: theory, experiment, application. Phys. Rep. **196**, 135 (1990). https://doi.org/10.1016/0370-1573(90)90040-9
29. W. Shi, T. Bartsch, C. Böhme, C. Brandau, A. Hoffknecht, H. Knopp, S. Schippers, A. Müller, C. Kozhuharov, F. Bosch, B. Franzke, P.H. Mokler, M. Steck, T. Stöhlker, Z. Stachura, Rate enhancement in the recombination of Bi^{80+} ions with electrons. Phys. Rev. A **66**, 022718 (2002). https://doi.org/10.1103/PhysRevA.66.022718
30. A. Hoffknecht, C. Brandau, T. Bartsch, C. Böhme, H. Knopp, S. Schippers, A. Müller, C. Kozhuharov, K. Beckert, F. Bosch, B. Franzke, A. Krämer, P.H. Mokler, F. Nolden, M. Steck, T. Stöhlker, Z. Stachura, Recombination of bare Bi^{83+} ions with electrons. Phys. Rev. A **63**, 012702 (2001). https://doi.org/10.1103/PhysRevA.63.012702
31. I.P. Grant, Relativistic atomic structure calculations. Comput. Phys. Commun. **17**, 149 (1979). https://doi.org/10.1016/0010-4655(79)90077-8
32. I.P. Grant, Relativistic calculation of atomic structures. Adv. Phys. **19**, 747 (1970). https://doi.org/10.1080/00018737000101191
33. K.G. Dyall, I.P. Grant, C.T. Johnson, F.A. Parpia, E.P. Plummer, GRASP: a general-purpose relativistic atomic structure program. Comput. Phys. Commun. **55**, 425 (1989). https://doi.org/10.1016/0010-4655(89)90136-7
34. F.A. Parpia, C.F. Fischer, I.P. Grant, GRASP92: a package for large-scale relativistic atomic structure calculations. Comput. Phys. Commun. **94**, 249 (1996). https://doi.org/10.1016/0010-4655(95)00136-0
35. J. Eichler, W.E. Meyerhof, *Relativistic Atomic Collisions* (Academic Press, Sabn Diego, 1995)
36. P. Zimmerer, N. Grün, W. Scheid, Auger rates for dielectronic recombination cross sections with highly charged relativistic heavy ions. Phys. Lett. A **148**, 457 (1990). https://doi.org/10.1016/0375-9601(90)90499-E
37. M. Zimmermann, N. Grün, W. Scheid, Photorecombination on highly charged few-electron uranium ions. J. Phys. B **30**, 5259 (1997). https://doi.org/10.1088/0953-4075/30/22/021
38. Z. Harman, C. Shah, A.J. González Martínez, U.D. Jentschura, H. Tawara, C.H. Keitel, J. Ullrich, J.R. Crespo López-Urrutia, Resonance strengths for KLL dielectronic recombination of highly charged mercury ions and improved empirical Z-scaling law. Phys. Rev. A **99**, 012506 (2019). https://doi.org/10.1103/PhysRevA.99.012506
39. S. Fritzsche, A fresh computational approach to atomic structures, processes and cascades. Comput. Phys. Commun. **240**, 1 (2019). https://doi.org/10.1016/j.cpc.2019.01.012
40. S. Fritzsche, P. Palmeri, S. Schippers, Atomic cascade computations. Symmetry **13**, 520 (2021). https://doi.org/10.3390/sym13030520
41. S. Fritzsche, Dielectronic recombination strengths and plasma rate coefficientsof multiply charged ions. Astron. Astrophys. **656**, A163 (2021). https://doi.org/10.1051/0004-6361/202141673
42. G. Visentin, S. Schippers, S. Fritzsche, Dielectronic recombination plasma rate coefficients of Na-, Mg-, and Al-like iron ions: The role of the $2(s+p) \rightarrow 4l, nl'$ and $3(s+p) \rightarrow 5l, nl'$ resonances. Astron. Astrophys. **679**, A13 (2023). https://doi.org/10.1051/0004-6361/202347456
43. V.M. Shabaev, I.I. Tupitsyn, V.A. Yerokhin, Model operator approach to the Lamb shift calculations in relativistic many-electron atoms. Phys. Rev. A **88**, 012513 (2013). https://doi.org/10.1103/PhysRevA.88.012513
44. W. Shi, S. Böhm, C. Böhme, C. Brandau, A. Hoffknecht, S. Kieslich, S. Schippers, A. Müller, C. Kozhuharov, F. Bosch, B. Franzke, P.H. Mokler, M. Steck, T. Stöhlker, Z. Stachura, Recombination of U^{92+} ions with electrons. Eur. Phys. J. D **15**, 145 (2001). https://doi.org/10.1007/s100530170160
45. N.R. Badnell, M.S. Pindzola, Unified dielectronic and radiative recombination cross sections for U^{90+}. Phys. Rev. A **45**, 2820 (1992). https://doi.org/10.1103/PhysRevA.45.2820
46. D.A. Knapp, P. Beiersdorfer, M.H. Chen, J.H. Scofield, D. Schneider, Observation of interference between dielectronic recombination and radiative recombination in highly charged uranium ions. Phys. Rev. Lett. **74**, 54 (1995). https://doi.org/10.1103/PhysRevLett.74.54
47. S. Schippers, S. Kieslich, A. Müller, G. Gwinner, M. Schnell, A. Wolf, M. Bannister, A. Covington, L.B. Zhao, Interference effects in the photorecombination of argonlike Sc^{3+} ions: Storage ring experiment and theory. Phys. Rev. A **65**, 042723 (2002). https://doi.org/10.1103/PhysRevA.65.042723
48. A.J. González Martínez, J.R. Crespo López-Urrutia, J. Braun, G. Brenner, H. Bruhns, A. Lapierre, V. Mironov, R. Soria Orts, H. Tawara, M. Trinczek, J. Ullrich, J.H. Scofield, State-selective quantum interference observed in the recombination of highly charged $Hg^{75+-78+}$ mercury ions in an electron beam ion trap. Phys. Rev. Lett. **94**, 203201 (2005). https://doi.org/10.1103/PhysRevLett.94.203201
49. N. Nakamura, N. Numadate, S. Oishi, X.M. Tong, X. Gao, D. Kato, H. Odaka, T. Takahashi, Y. Tsuzuki, Y. Uchida, H. Watanabe, S. Watanabe, H. Yoneda, Strong polarization of a $J = 1/2$ to $1/2$ transition arising from unexpectedly large quantum interference. Phys. Rev. Lett. **130**, 113001 (2023). https://doi.org/10.1103/PhysRevLett.130.113001

50. L. Landau, E.M. Lifshitz, *Course of Theoretical Physics Volume 2 - The classical theory of fields* (Butterworth–Heinemann, Oxford, UK, 1994). https://archive.org/details/landau-and-lifshitz-physics-textbooks-series/
51. M. Lestinsky, V. Andrianov, B. Aurand, V. Bagnoud, D. Bernhardt, H. Beyer, S. Bishop, K. Blaum, A. Bleile, A. Borovik, F. Bosch, C.J. Bostock, C. Brandau, A. Bräuning-Demian, I. Bray, T. Davinson, B. Ebinger, A. Echler, P. Egelhof, A. Ehresmann, M. Engström, C. Enss, N. Ferreira, D. Fischer, A. Fleischmann, E. Förster, S. Fritzsche, R. Geithner, S. Geyer, J. Glorius, K. Göbel, O. Gorda, J. Goullon, P. Grabitz, R. Grisenti, A. Gumberidze, S. Hagmann, M. Heil, A. Heinz, F. Herfurth, R. Heß, P.M. Hillenbrand, R. Hubele, P. Indelicato, A. Källberg, O. Kester, O. Kiselev, A. Knie, C. Kozhuharov, S. Kraft-Bermuth, T. Kühl, G. Lane, Y.A. Litvinov, D. Liesen, X. Ma, R. Märtin, R. Moshammer, A. Müller, S. Namba, P. Neumeyer, T. Nilsson, W. Nörtershäuser, G. Paulus, N. Petridis, M. Reed, R. Reifarth, P. Reiß, J. Rothhardt, R. Sanchez, M.S. Sanjari, S. Schippers, H.T. Schmidt, D. Schneider, P. Scholz, R. Schuch, M. Schulz, V. Shabaev, A. Simonsson, J. Sjöholm, O. Skeppstedt, K. Sonnabend, U. Spillmann, K. Stiebing, M. Steck, T. Stöhlker, A. Surzhykov, S. Torilov, E. Träbert, M. Trassinelli, S. Trotsenko, X.L. Tu, I. Uschmann, P.M. Walker, G. Weber, D.F.A. Winters, P.J. Woods, H.Y. Zhao, Y.H. Zhang, Physics book: CRYRING@ESR. Eur. Phys. J. ST **225**, 797 (2016). https://doi.org/10.1140/epjst/e2016-02643-6
52. M. Lestinsky, E.B. Menz, H. Danared, C. Krantz, E. Lindroth, Z. Andelkovic, C. Brandau, A. Bräuning-Demian, S. Fedotova, W. Geithner, F. Herfurth, A. Kalinin, I. Kraus, U. Spillmann, G. Vorobyev, T. Stöhlker, First experiments with CRYRING@ESR. Atoms **10**, 141 (2022). https://doi.org/10.3390/atoms10040141
53. C. Møller , General properties of the characteristic matrix in the theory of elementary particles. Det Kgl. Danske Vid. Selsk. Mat.-Fys Medd. **23**, 1 (1945)
54. M. Cannoni, Lorentz invariant relative velocity and relativistic binary collisions. Int. J. Mod. Phys. A **32**, 1730002 (2017). https://doi.org/10.1142/S0217751X17300022
55. A. Müller, Plasma rate coefficients for highly charged ion-electron collisions: new experimental access via ion storage rings. Int. J. Mass Spectrom. **192**, 9 (1999). https://doi.org/10.1016/S1387-3806(99)00098-6
56. A. Hoffknecht, T. Bartsch, S. Schippers, A. Müller, N. Eklöw, P. Glans, M. Beutelspacher, M. Grieser, G. Gwinner, A.A. Saghiri, A. Wolf, Recombination of F^{6+} with free electrons at low energies. Phys. Scr. **T80**, 298 (1999). https://doi.org/10.1238/Physica.Topical.080a00298
57. S. Schippers, M. Schnell, C. Brandau, S. Kieslich, A. Müller, A. Wolf, Experimental Mg IX photorecombination rate coefficient. Astron. Astrophys. **421**, 1185 (2004). https://doi.org/10.1051/0004-6361:20040380
58. R.A. Treumann, W. Baumjohann, Anisotropic Jüttner (relativistic Boltzmann) distribution. Ann. Geophys. **34**, 737 (2016). https://doi.org/10.5194/angeo-34-737-2016
59. A. Lampert, A. Wolf, D. Habs, J. Kenntner, G. Kilgus, D. Schwalm, M.S. Pindzola, N.R. Badnell, High-resolution measurement of the dielectronic recombination of fluorinelike selenium ions. Phys. Rev. A **53**, 1413 (1996). https://doi.org/10.1103/PhysRevA.53.1413
60. W. Spies, A. Müller, J. Linkemann, A. Frank, M. Wagner, C. Kozhuharov, B. Franzke, F. Bosch, H. Eickhoff, M. Jung, O. Klepper, W. König, P.H. Mokler, R. Moshammer, F. Nolden, U. Schaaf, P. Spädtke, M. Steck, P. Zimmerer, N. Grün, W. Scheid, M.S. Pindzola, N.R. Badnell, Dielectronic and radiative recombination of lithiumlike gold. Phys. Rev. Lett. **69**, 2768 (1992). https://doi.org/10.1103/PhysRevLett.69.2768
61. C. Brandau, Messungen zur Photorekombination hochgeladener lithiumähnlicher Ionen. Ph.D. thesis, Justus-Liebig-Universität, Gießen (2000). http://geb.uni-giessen.de/geb/volltexte/2001/407/
62. D. Paul, M. Grieser, F. Grussie, R. von Hahn, L.W. Isberner, Á. Kálosi, C. Krantz, H. Kreckel, D. Müll, D.A. Neufeld, D.W. Savin, S. Schippers, P. Wilhelm, A. Wolf, M.G. Wolfire, O. Novotný, Experimental determination of the dissociative recombination rate coefficient for rotationally-cold CH^+ and its implications for the diffuse cloud chemistry. Astrophys. J. **939**, 122 (2022). https://doi.org/10.3847/1538-4357/ac8e02
63. A. Kálosi, M. Grieser, R. von Hahn, U. Hechtfischer, C. Krantz, H. Kreckel, D. Müll, D. Paul, D.W. Savin, P. Wilhelm, A. Wolf, O. Novotný, Laser probing of the rotational cooling of molecular ions by electron collisions. Phys. Rev. Lett. **128**, 183402 (2022). https://doi.org/10.1103/PhysRevLett.128.183402
64. D. Bernhardt, Dielektronische Rekombination lithium- und berylliumartiger Xenonionen am Schwerionenspecherring ESR. Dissertation, Justus-Liebig-University Giessen (2012), http://geb.uni-giessen.de/geb/volltexte/2012/8909/
65. D. Bernhardt, C. Brandau, Z. Harman, C. Kozhuharov, S. Böhm, F. Bosch, S. Fritzsche, J. Jacobi, S. Kieslich, H. Knopp, F. Nolden, W. Shi, Z. Stachura, M. Steck, T. Stöhlker, S. Schippers, A. Müller, Electron-ion collision spectroscopy: lithium-like xenon ions. Phys. Rev. A **91**, 012710 (2015). https://doi.org/10.1103/PhysRevA.91.012710